Local atomic structure in cubic stabilized zirconia

P. Villella, S. D. Conradson, F. J. Espinosa-Faller, S. R. Foltyn, K. E. Sickafus, and J. A. Valdez
Materials Science and Technology Division, Los Alamos National Laboratory, New Mexico 87545

C. A. Degueldre
LWV, Paul Scherrer Institute, 5232 Villigen-PSI, Switzerland

(Received 8 February 2001; revised manuscript received 22 May 2001; published 7 August 2001)

X-ray-absorption fine structure measurements have been used to elucidate the local atomic structure of quaternary Zr, Y, Er, Ce/U cubic stabilized zirconia. These compounds display more complicated local environments than those reported for simpler binary systems. While the shortest cation-O distances are similar to those found in the binary cubic stabilized compounds, responding to the different sizes of the cations, we have identified large distortions in the first-shell oxygen distribution involving long, 2.8–3.2 Å cation-O distances that are similar to those found in the amorphous phase of zirconium. The cation-cation distributions are also found to be quite complicated (non-Gaussian) and element specific. The U-near neighbor distances are expanded relative to the Ce ions for which it substitutes, consistent with the larger size of the actinide, and the U-cation distribution is also more complicated. In terms of the effects of this substitution on the other cation sites, the local environment around Y is altered while the Zr and Er local environments remain unchanged. These results point out the importance of collective and correlated interactions between the different pairs of cations and the host lattice that are mediated by the local strain fields generated by the different cations. The presence of pair-specific couplings has not been commonly included in previous analyses and may have implications for the stabilization mechanisms of cubic zirconia.

DOI: 10.1103/PhysRevB.64.104101 PACS number(s): 61.10.Ht, 61.72.Ji, 61.72.Ww, 61.43.−j

I. INTRODUCTION

The zirconia phase and its dependence upon the complicated and delicate balance between the geometry of the ZrO_{7-8} cluster, the number of nearest neighbor (NN) oxygen atoms, the Zr-O distance, and local strain[1] demonstrate the need for accurate and complete atomic scale structural characterization of cubic stabilized zirconia (CSZ). If the dopants in their different local environments behave as separate, independent entities then their effects on the structure and its stability will be cumulative, linear, and easily predictable. If the dopants interact or participate in collective behavior then complex, nonlinear, and even discontinuous or critical types of behavior are possible. A related phenomena in complex materials and quite possibly CSZ is nanoscale heterogeneity or phase separation[2–5] and its association with interesting correlated behaviors of electrons and atoms (e.g., high-temperature superconductivity,[6,7] and colossal magnetoresistance[8]). Heterogeneity or phase separation of atoms could be driven by nanoscale defect aggregation and fluctuations in composition, local strain, and/or charge. This may occur naturally because of the random distribution of substitutional elements in nonstoichiometric compounds, but may also result or be enhanced by collective interactions among isolated defect sites that cause the formation of aperiodic clusters or networks. The small size of these domains (at or below the diffraction limit) as well as their poor coherence prevent them from diffracting even while they may comprise a significant portion of the material.

Phase stability is the primary concern in the zirconia system. Zr and Hf dioxides are unique among transition metals in displaying a cubic fluorite instead of a rutile-type structure. This unusual behavior can be attributed to the high charge-to-radius ratio for Zr^{4+}, which promotes short, highly covalent, seven-coordinate Zr-O bonding[1] and results in a high degree of flexibility and disorder in the local atomic environment around Zr. Six polymorphs, all of which can be considered topologically identical derivatives of the fluorite structure via displacive movements of the O and Zr atoms, have been described for ZrO_2, with the monoclinic, tetragonal, and cubic phases stable at ambient pressure. Seven-coordinate Zr in the monoclinic phase displays seven unique oxygen sites with a mean Zr-O bond distance of 2.16 Å.[9] The Zr coordination becomes eightfold in the higher symmetry structures with an expansion of the average Zr-O distance from 2.16 Å to 2.26–2.28 Å.[10,11] The high-temperature cubic and tetragonal phases are stabilized at room temperature by the substitution of Zr^{4+} with relatively large concentrations of other, aliovalent cations (e.g., Mg^{2+}, Ca^{2+}, Y^{2+}). These dopants introduce oxygen vacancies into the lattice and reduce the Zr coordination in the cubic phase with concomitant diminution of the average Zr-O distance in both the tetragonal and cubic phases.[12–16] Thermodynamically, the cubic phase is fully stable only when the average Zr coordination is ~7.5,[1,7–19] consistent with ZrO_7 clusters as the favored cubic geometry. Although consensus was not immediate,[11,20–25] X-ray-absorption fine structure (XAFS) measurements by Li *et al.*[17–19] indicate and calculations support[26] O vacancies NN to Zr when the aliovalent dopant cation is larger than Zr and NN to the dopant when it is smaller than Zr, consistent with the observation that smaller cations are less effective stabilizers.[27,28]

Crystallographic approaches, while providing the essential information on the average structure, are not as effective as local structure measurements in characterizing these mechanisms even when conventional analysis of Bragg

peaks is augmented with, e.g., Fourier difference maps[29] and diffuse scattering analysis.[30,31] The elemental specificity of XAFS is part of its advantage, but the sensitivity of scattering to the long-range average structure of the coherent fraction of the crystal and its bias towards periodicity and symmetric structures have produced what are likely to be overly simplistic structural models for CSZ. In particular the cation disorder has been very difficult to describe in the crystallographic context with the majority of studies using identical cation sites with randomly distributed dopants.[12,29–37] Some investigations have identified displacements of the cations in CSZ.[12,30] The vast majority, however, have focused on the displacements of the oxygen atoms NN to oxygen vacancies and pairing/interactions of vacancies,[29–33] size effect strains,[34,35] and the possible presence on anharmonic thermal vibrations.[36] The primary focus on oxygen displacements and the ordering/interaction of oxygen vacancies has resulted in a picture in which oxygen atoms NN to vacancies, and neighboring cations to a lesser extent, are simply displaced from the ideal fluorite positions along lattice vectors.[38] These models lack the site-specific details provided by XAFS that are essential in understanding the mechanisms of tetragonal and cubic stabilization with different classes of substituent cations. CSZ's cannot be understood in the context of the ''average structure'' approach inherent to diffraction-based crystallographic methods. They require ''local structure'' information that describes the differences in the behavior of the different cations. This is corroborated by calculations that also show distinct ordering preferences for oxygen vacancies and much more extensive site-specific but aperiodic displacements of all of the atoms in response to this ordering.[26] These supercell calculations for isolated defects indicate that oxygen and cation atoms NN to vacancies can experience off-lattice-vector displacements as large as 0.30 and 0.20 Å, respectively.

In addition to determining that the preferred location of oxygen vacancies is NN to the smaller cation (often Zr), XAFS studies of local structure in zirconia elucidated other significant trends. The radial geometry of the MO_{6-8} (where M indicates a metal cation) clusters in a given phase is specific to the different cations but independent of the composition,[19,27] in contradiction to diffraction results. Additionally, these previous XAFS studies find that for equal sized and larger dopants the Fourier transform amplitude of the second-shell cations decreases with increasing dopant concentration[19,28] even while good fitting results are still obtained with a single, Gaussian shell. Since the occupancy for this site must be conserved, this implies that, as expected for differently structured local environments, the cation distribution is becoming increasingly disordered as the number of different types of sites, i.e., $M_0Zr_{12}, M_1Zr_{11}, M_2Zr_{10}$, etc., increases. This contribution to the XAFS continues to be well fit with the simple, single-distance, Gaussian distribution model. However, high-quality fits are only a necessary but not sufficient criterion for the accuracy of a result because of uniqueness problems and biases that afflict XAFS similarly to diffraction. For example, the NN oxygen of several zirconia polymorphs was well fit with a single, Gaussian oxygen shell, giving accurate average distances and relative widths vis-à-vis crystallographic results. However, the reported crystallographic data indicate that the distributions are far from Gaussian and the separations between positions are often greater than the resolution limit of the data.[17] In addition, the possible importance of collective interactions between the different cation sites has been hinted at not only in the case of small cations but also for the Zr-Y-Nb-O system. A preference of the Nb to be next NN to Y suggests that the scale of charge compensation is subnanometer, occurring via the interactions of adjacent atoms rather than averaged over the crystal.[28]

We have addressed these issues in CSZ's for inert matrix fuel (IMF) applications by performing Zr, Y, Er, and Ce/U XAFS measurements on a series of related compounds of the form $Zr_xY_yEr_z(Ce/U)_sO_{2-\delta}$ (δ is determined by the content of Y and Er). The analysis was focused on the complete elucidation of the element-specific pair distribution function to determine if the trends reported for simpler compounds continue in these more complicated systems. In addition, identifying different dependencies of the local environment of the different cations on the overall composition will provide an indication of the importance of possible complex and cooperative behavior between the different cation species in CSZ. Our results will show that there are specific ways in which each cation distorts its surrounding atomic environment and that some of the cations participate in pair-specific interactions that may ultimately have ramifications on the proposed stabilization mechanisms and structural models for CSZ.

II. EXPERIMENT

$Er_{0.05}Y_{0.10}Zr_{0.85}O_{1.92}$, $Er_{0.05}Y_{0.10}Ce_{0.10}Zr_{0.75}O_{1.92}$, $Er_{0.07}Y_{0.10}Ce_{0.15}Zr_{0.68}O_{1.91}$, $Er_{0.05}Y_{0.15}Ce_{0.10}Zr_{0.70}O_{1.90}$, and $Er_{0.05}Y_{0.10}U_{0.10}Zr_{0.75}O_{1.92}$ were obtained by coprecipitation of their oxy-hydroxides by ammonia addition to nitrate solution of the metal salts. The cake was dried, calcined, and milled to produce the oxide powder. The sample containing uranium was dried under an inert atmosphere to avoid oxidation. Aliquots of these powders were pressed prior to sintering of the pellets at 1600 °C for 5 h. Pellets were milled prior to x-ray analysis. For spectroscopic measurements, samples were manually ground with a mortar and pestle and loaded into 2.5×20 mm slots in an aluminum holder attached to the cryostat coldfinger.

X-ray diffraction measurements on the $Er_{0.05}Y_{0.10}Zr_{0.85}O_{1.92}$ sample[39] confirm its cubic structure with a lattice parameter $a=5.135\pm 0.002$ Å that is slightly larger than that of pure cubic zirconia ($a=5.120\pm 0.005$ Å).[40] The addition of Ce expands the lattice parameter to $a=5.174\pm 0.007$ Å in the $Er_{0.05}Y_{0.10}Ce_{0.10}Zr_{0.75}O_{1.92}$ sample and substitution of U for Ce again slightly expands the lattice parameter to $a=5.179\pm 0.007$ Å. The diffraction showed that all samples were single phase.

The x-ray absorption spectra were measured at the Stanford Synchrotron Radiation Laboratory on beamline 4-2 using Si(220) and Si(440) monochromator crystals. The relative orientation of the monochromator crystals was tuned to maximize x-ray flux. Harmonic rejection was achieved with

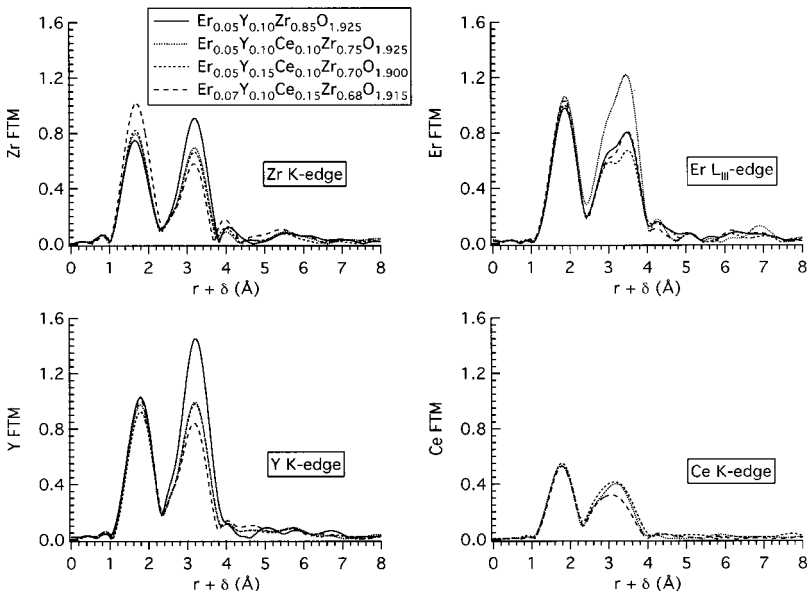

FIG. 1. The Fourier transform moduli (FTM's) of XAFS data collected for each of the cations present in the IMF compounds. These moduli are shown over an abbreviated range of the *k*-space data ($k=3.0-10.0$ Å^{-1}) since taking a larger range obscures differences in the second-shell cation peaks (the disordered contribution is masked by the much stronger Gaussian contribution that dominates at higher *k* values). The first peak due to the *M*-O is insensitive to the total dopant concentration with the exception of the Zr data. The *M*-*M* distribution shows marked differences for each data set indicating that the local atomic distribution of cations differ around Zr, Y, Er, and Ce.

a Pt-coated mirror. The absorption spectra were measured across the *K* edge for Zr, Y, and Ce and across the L_{III} edge for Er and U. The spectra were obtained through fluorescence spectroscopy by averaging the signal from each of 9–11 elements of a Ge fluorescence detector. All data were measured at 80 K using a liquid nitrogen cryostat. The spectra were collected up to an energy corresponding to $k=15$ Å^{-1} for each element. The XAFS for each spectrum were extracted using standard methods.[41] The energy was calibrated by defining the first inflection point of the absorption edge to be that of the pure element. The energies used are 17.998 keV for the Zr *K* edge, 17.038 for the Y *K* edge, 40.443 keV for the Ce *K* edge, 8.358 keV for the Er L_{III} edge, and 17.166 keV for the U L_{III} edge. Normalized data were obtained by setting the difference between preedge and postedge polynomial fits to the spectra to unity. The XAFS were obtained as the difference between the spectra and a polynomial spline fit to the postedge region. The spline was adjusted to minimize the integrated area under the low-frequency region ($r<1.0$ Å) in the corresponding Fourier transform.

Metrical parameters of interest were obtained by nonlinear least squares fitting of the k^3-weighted XAFS data over the range $k=3.0-14.2$ Å^{-1}, with the exception of the U data in which the fit was performed up to $k_{\max}=13$ Å^{-1}. The focus of this study was on identifying the existence and location of shells of neighbor atoms, the sum of which define the (partial) radial distribution functions. Theoretical scattering phases and amplitudes needed for the curve fits were calculated with the FEFF7 code.[42] The complicated distributions that were found obscure the numbers of atoms and their Debye-Waller factors. Evaluation of selected amplitude parameters was performed by ratioing and subtraction methods. Similarly, the possibility of four types of overlapping cation neighbors that do not necessarily match the stoichiometry let us to present these second-neighbor results as a single composite distribution function. Additional details of our fitting procedure are described in the next section.

The results of the XAFS measurements are shown in the form of Fourier transform magnitudes (FTM). The distances observed in the FTM are shifted to smaller distances from the true bond distances by the x-ray scattering phase shift that is a function of the absorber-scatterer pair. The FTM contains only half of the information content of the XAFS spectrum. The combination of the strike imaginary/real components of the FTM [analogous to the phase in $\chi(k)$] provide both the sensitivity to the neighbor atoms' atomic number as well as details of the distribution that are obscured by interference and overlap in the FTM.

III. RESULTS AND DISCUSSION

The FTM's for the extracted XAFS data all show two prominent peaks indicative of a quasicubic local structure (Fig. 1). The first peak in each FTM is due to the *M*-O distribution (where $M=$ Zr, Y, Er, Ce) while the second is due to the *M*-*M* distribution. The small contributions around and just above 4 Å in the plots are due to the third NN *M*-O contributions lying beyond the *M*-*M* distances in the fluorite structure. The FTM's of Fig. 1 are taken over $k=3-10$ Å^{-1}, a shorter range than used for the curve fits. This short range accentuates the differences between the spectra, a counterintuitive effect that we believe reflects rapid damping of the contributions from the disordered components of the structure.

The Zr-O peak located at $r+\delta=1.6$ Å shows enhanced amplitude as a function of total dopant concentration. This behavior is not typical of nonstoichiometric compounds in which we expect disorder to reduce the peak amplitudes as the dopant concentration increases. The remaining *M*-O peaks, which are shifted by 0.2 Å to $r+\delta=1.8$ Å in their respective FTM's, show a relatively insensitive response to the total dopant concentration. The normal trend of decreasing oxygen peak amplitude as the atomic number of the central absorbing atom increases is not reflected in these data. The absence of this trend indicates that there are additional factors making significant contributions to the peak amplitudes such as static disorder or more likely the presence of

the multiple, cation-dependent *M*-O distances we have identified.

The *M*-*M* peaks, nominally located at $r+\delta=3.2$ Å in each of the spectra, show concentration dependence for all data sets. The general trend is a decrease in the *M*-*M* peak amplitude as a function of total dopant concentration except in the case of the Er data in which this peak is split and shows a nonmonotonic change in amplitude with increasing dopant concentration. In the cases of Zr and Y the *M*-*M* peak displays a small shoulder on the low-*r* side and the Ce-*M* peak is quite broad with a highly reduced amplitude. These features reinforce the idea that the cation distribution is more complex than can be accounted for by a simple Gaussian distribution and random chemical ordering. There are no appreciable spectral contributions above $r+\delta=4.5$ Å in any of the FTM's indicating the loss of extended local order in these compounds with a more complicated composition relative to simpler binary CSZ compounds.

Previous XAFS studies on CSZ and its many polymorphs used a single Gaussian shell to characterize the oxygen and cation contributions and achieved good fits that identified Zr-O and Zr-*M* distances and Gaussian widths in agreement with the average crystallographic values.[17–19,27,28,43] The Zr-O and Zr-*M* distributions, however, are far from Gaussian, so it is more accurate to describe these results as depicting the Gaussian component of the local atomic distribution. Characterizing all of the details of a complicated, asymmetric, multisite distribution is difficult because there is no generalized method applicable to XAFS spectra. Attempting to use a sum of several Gaussians quickly leads to an overdetermined fit with too many parameters. We have had success with this problem by performing a series of both limited and overdetermined fits on all spectra from related compounds. We have also found it more effective to use the resulting radial distribution function (RDF) with its overlapping shells to provide a qualitative picture of the local environment rather than the metrical parameters resulting from the fit.[44] Inherent to such a procedure is the necessity of proving that the additional shells giving the asymmetry actually do exist and are not artifacts of a potentially overdetermined fit. This is accomplished by comparing the residuals (data minus fit) over multiple spectra from related compounds, and examining these differences for consistently appearing features that are well fit by the type of atom in question. We will discuss the details of this procedure in the case of the Zr *K*-edge XAFS data in order to explicitly show our methodology that is critical to identifying all the shells of atoms and components of the distributions.

This process was begun by closely comparing the Zr *K*-edge FTM of the IMF compounds with that of a pure cubic zirconia thin film obtained by ion beam irradiation of a monoclinic thin film. Of more interest than the difference in amplitude was the fact that the IMF compounds show a small but consistently resolved peak at $r=2.2$ Å whereas the cubic ZrO_2 simply displays a broadening of the baseline (Fig. 2, upper panel). The Zr-O distribution of the cubic ZrO_2 standard was well fit by two or three oxygen shells with Zr-O bond distances less than 2.7 Å while the Zr-O distribution of the IMF compounds was not. When these initial limited fits

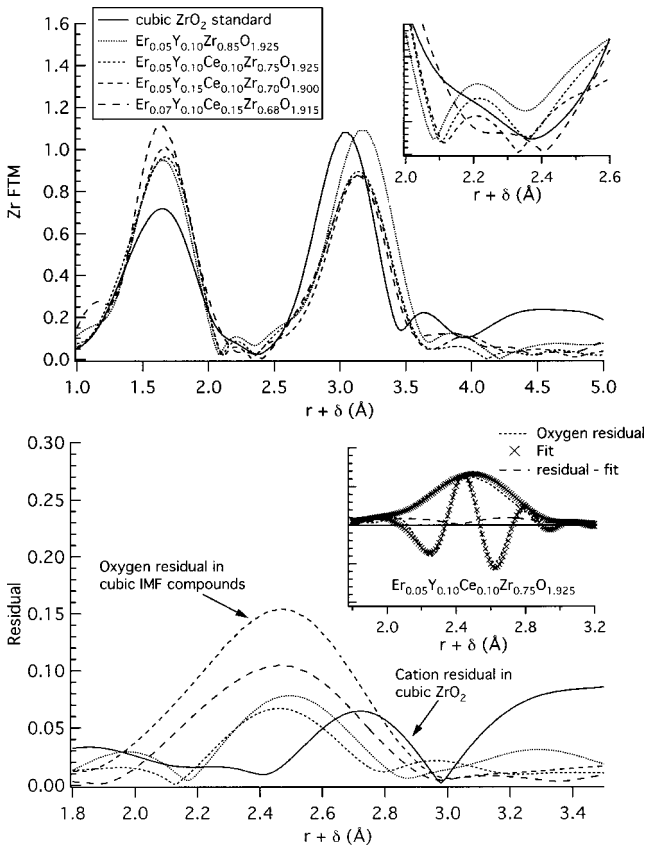

FIG. 2. Upper panel: The FTM ($k=3.0-14.25$ Å^{-1}) of the Zr *K*-edge XAFS for the monoclinic (standard) and Zr-Y-Er-Ce zirconias. The inset shows how the spectrum of the monoclinic standard significantly differs from those of the more complicated compounds in the region between the two main peaks. This difference originates in the presence of a complicated, multisite oxygen NN distribution consisting of oxygen shells with Zr-O distances greater than 2.7. Lower panel: The fit residuals (data-fit) display significant spectral features at 2.5 when oxygen contributions beyond 2.7 are neglected. A two oxygen NN fit to the monoclinic standard shows no additional oxygen contributions (the peak at 2.7 is due to a disordered/multisite Zr-*M* contribution). The inset shows a fit to this additional oxygen contribution and displays an excellent phase and amplitude match with the oxygen standard generated by FEFF7.

are subtracted from the data, the residuals exhibit a peak at $r+\delta=2.5$ Å. This feature is subsequently well fit by additional oxygen shells (Fig. 2, lower panel). The reproducibility of this feature across the related IMF compounds as well as the excellent phase and amplitude match of the oxygen fit to the residual increase our confidence that the residual is indeed due to an oxygen contribution (inset to Fig. 2, lower panel). These results imply the presence of Zr-O distances greater than 2.7 Å in the IMF compounds, as have been reported in amorphous zirconia.[45] We have applied this method of analysis to the oxygen and cation contributions for each of the IMF compounds for each absorption edge resulting in the RDF's depicted in Fig. 3.

In addition to our curve fitting analysis we have used the ratio method[41] in order to further characterize the back transform amplitudes of the first shell *M*-O distribution. This method allows a sensitive comparison of the coordination

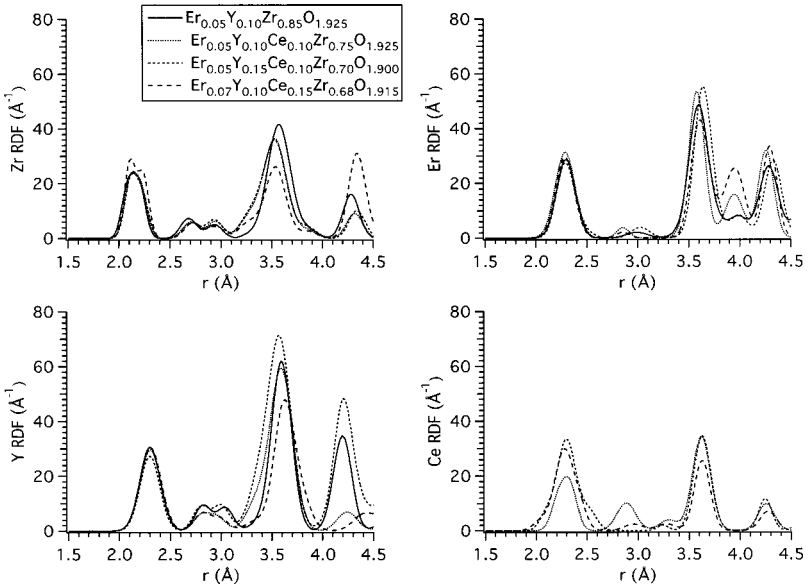

FIG. 3. The radial distribution functions (RDF's) resulting from the curve fitting procedure described in the text. The first-shell oxygen contributions (1.9–2.5) are multisite for the Zr and Ce, and highly ordered and single site for Y and Er. Zr, Y, and the Ce compound with the lowest Ce concentration all show a complex oxygen distribution lying between 2.5 and 3.1 that is split in the Zr and Y data. All data sets show a complex disordered *M-M* distribution lying between 3.2 and 4.0 with the Er RDF showing a well-resolved splitting of the cation shell. Contributions lying above 4.1 are due to third-shell oxygen atoms that occur in the cubic fluorite structure.

numbers for the absorbing atom as a function of the sample composition. This method is comparative; the results are obtained as changes with respect to a reference sample, and so has only minimal dependence on the fitting procedure. Changes in the functional form of the amplitude ratio are an indication of changes in the local atomic environment of the absorbing atoms with respect to the reference material. Ideally, the form of the amplitude ratios should be linear as a function of k, and for simple Gaussian shells with identical Debye-Waller factors the ratio will be a horizontal line. Departures from linearity are an indication that the distributions of the reference and sample in question are different (i.e., differing Debye-Waller factors or Gaussian vs non-Gaussian distributions).

A. Zr-O

The average *M*-O and *M-M* distances are quite typical of CSZ; however, the curve fitting results indicate a more complicated picture of the local atomic structure surrounding each element (Fig. 3). Substantial dependence of the oxygen NN distribution on the central atom is found. The NN oxygen distribution of Zr is found to be split between two sites with an average separation of 0.12 Å (Table I) and a mean Zr-O distance of 2.17 Å. This mean Zr-O distance and the splitting is consistent with diffraction measurements on CSZ.[12] The splitting and relative spectral weights are weakly dependent on the total dopant concentration. However, a sharp increase in the total number is observed for the compound with the highest impurity concentration in agreement with the FTM's of Fig. 1. We have augmented the curve fitting analysis of the first-shell oxygen contributions by the ratio method. In this analysis we have used the backtransform amplitude of the $Er_{0.05}Y_{0.10}Zr_{0.85}O_{1.92}$ sample as a reference by assuming the coordination number for Zr to be 7 in accordance with its cubic stabilized structure. The results of the ratio analysis are then determined with respect to this assumed coordination.

The imaginary part and the amplitude of the backtransforms for the first-shell Zr-O contributions as well as the amplitude ratios are shown in Fig. 4. In the case of the Zr-O distribution the departure from linearity in the amplitude ratios, which is significant beyond $k=11\ \text{Å}^{-1}$, is caused by the beat in the backtransform that results from the interference of the two distances comprising this first shell. Linear fits to the amplitude ratio over the range $k=3-11\ \text{Å}^{-1}$ allow one to extract the change in coordination number if the distances and Debye-Waller factors from the curve fitting analysis are used as inputs. The distances and Debye-Waller factors used are those found in Table I for the Zr-O distribution (adjustment of the Debye-Waller factors from those found through the fitting process did not affect the results of the ratio process). The inset to Fig. 4 (lower panel) shows the results of the ratio analysis that show the apparent coordination number of Zr to be increasing by 13% as the total dopant con-

TABLE I. Curve fitting results for the Zr-O distributions. Typical errors are ±0.02 Å for the bond distances, ±20% for coordination numbers, and ±0.01 for the Debye-Waller factors.

	Zr-O (Å)	N	σ (Å)
$Er_{0.05}Y_{0.10}Zr_{0.85}O_{1.92}$	2.08, 2.20, 2.68, 2.94, 4.28	2.82, 2.77, 1.47, 1.00, 3.24	0.06, 0.06, 0.08, 0.08, 0.08
$Er_{0.05}Y_{0.10}Ce_{0.10}Zr_{0.75}O_{1.92}$	2.11, 2.22, 2.70, 2.95, 4.31	3.06, 2.47, 1.21, 1.24, 1.83	0.06, 0.06, 0.08, 0.08, 0.08
$Er_{0.05}Y_{0.15}Ce_{0.10}Zr_{0.70}O_{1.90}$	2.12, 2.23, 2.71, 2.94, 4.34	3.22, 2.16, 1.13, 1.37, 2.04	0.06, 0.06, 0.08, 0.08, 0.08
$Er_{0.07}Y_{0.10}Ce_{0.15}Zr_{0.68}O_{1.91}$	2.10, 2.23, 2.72, 2.94, 4.34	2.98, 3.54, 1.19, 0.99, 4.94	0.04, 0.05, 0.08, 0.08, 0.08
$Er_{0.05}Y_{0.10}U_{0.10}Zr_{0.75}O_{1.92}$	2.11, 2.24, 2.73, 2.96, 4.37	3.11, 2.10, 1.40, 1.94, 1.43	0.06, 0.06, 0.08, 0.08, 0.08

centration increases from 15 to 32 at. %. The error bars for the coordination are a reflection of the deviation of the amplitude ratio from the zero-slope fit and not an indication of the absolute error in coordination number. This result is surprising in that the coordination of Zr in the cubic phase is thought to be 7 independent of the dopant concentration, however, is consistent with the increasing Zr-O peak amplitude found in the Zr FTM (Fig. 1). This apparent increase in coordination could also result from a reduction in the disorder of the Zr-O distribution that is reflected in the larger numbers and smaller Debye-Waller factors found in the curve fits (Table I).

In addition to the split first-shell oxygen contributions we have identified, in the fit residuals from the single O shell fit, prominent sets of longer oxygen distances lying between 2.5 and 3.1 Å that are also split by 0.24 Å. The finding that there are Zr-O contributions in the range of 2.6–3.1 Å is supported by XAFS studies of amorphous ZrO_2 (a-ZrO_2) thin films. This study found that the Zr-O distribution in a-ZrO_2 is spread from 1.9 to 3.3 Å by using reverse Monte Carlo analysis[45] to deal with the significant disorder. The presence of these longer Zr-O distances could be an indication of complex defect structures and/or significant disorder induced by the complicated nonstoichiometric substitutions in these IMF compounds.

B. Y-O

The shortest Y-O contribution, unlike that of Zr-O, is well fit by a single Gaussian shell at 2.30 Å independent of total dopant concentration. The distances, coordination numbers, and Debye-Waller factors found in the curve fitting analysis (Table II) are consistent with the results of the local atomic structure found in simpler yttria-stabilized cubic zirconia.[18] This first shell was also analyzed by the ratio method (Fig. 5) in an effort to identify any change in Y coordination. Again the reference compound chosen was $Er_{0.05}Y_{0.10}Zr_{0.85}O_{1.92}$ and the coordination for the first-shell oxygen distribution was assumed to be 8 consistent with the curve fit results and previous XAFS studies. The results of this analysis indicate that the Y coordination changes by less than 10%, which is well within the uncertainty for coordination number in XAFS analysis. The amplitude ratio for the compound with the largest Y concentration has the strongest departure from linearity as well as the lowest coordination number. An additional analysis of the Y coordination can be made by using the first-shell Zr-O backtransform amplitude. In each case the reference used is the first-shell Zr-O contribution from each compound as well as the coordination numbers identified through the ratio analysis of the Zr coordination (Fig. 4). Where the previous ratio comparisons were a function of dopant concentration these ratios will compare the Zr and Y coordination with the same dopant concentration. The results of this analysis show that the Y coordination is on average greater than the Zr coordination by 1.28 and varies by less than 11% across the samples (Fig. 6). As in previous cases the deviations of the Y/Zr amplitude ratios from linearity result from the two-site nature of the Zr-O distributions vs

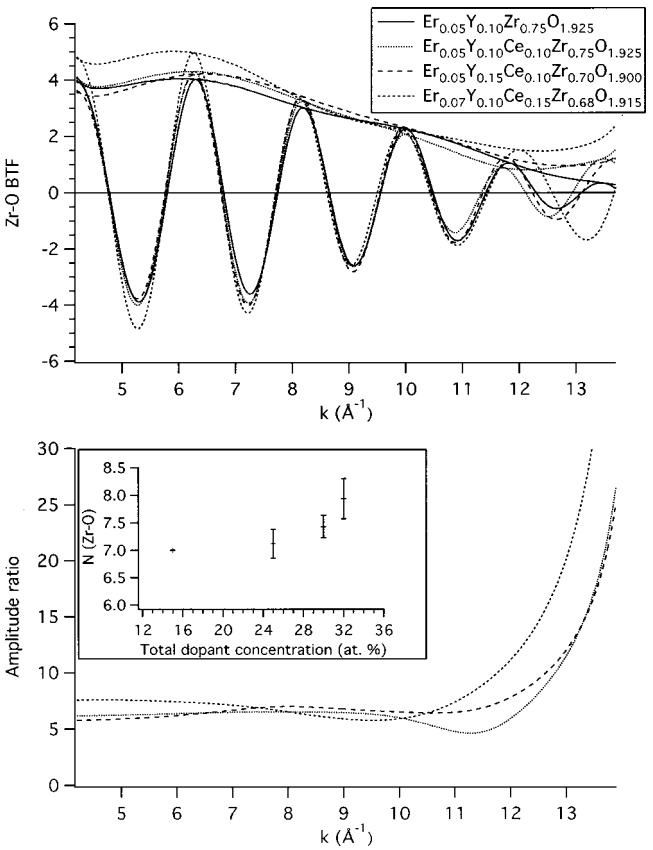

FIG. 4. Upper panel: The imaginary part and amplitude of the backtransform of the NN Zr-O shell showing evidence for a beat at 12.5 $Å^{-1}$ that results from the two-site distribution. Lower panel: The amplitude ratio functions also show evidence for a change in the bear near 12.5 $Å^{-1}$ indicating a change in the separation and/or spectral weights of the two shells comprising the NN Zr-O distribution. The inset shows results of the coordination analysis of the amplitude ratios indicating a possible increase in the Zr coordination number by 13%.

TABLE II. Curve fitting results for the Y-O distributions. Typical errors are ±0.02 Å for the bond distances, ±20% for coordination numbers, and ±0.01 for the Debye-Waller factors.

	Y-O (Å)	N	σ (Å)
$Er_{0.05}Y_{0.10}Zr_{0.85}O_{1.92}$	2.30, 2.82, 3.04, 4.19	7.66, 1.89, 1.71, 7.31	0.10, 0.08, 0.08, 0.09
$Er_{0.05}Y_{0.10}Ce_{0.10}Zr_{0.75}O_{1.92}$	2.30, 2.81, 2.97, 4.24	7.54, 1.18, 0.99, 1.74	0.10, 0.08, 0.08, 0.10
$Er_{0.05}Y_{0.15}Ce_{0.10}Zr_{0.70}O_{1.90}$	2.30, 2.80, 3.00, 4.20	6.62, 1.78, 1.87, 5.46	0.10, 0.08, 0.08, 0.08
$Er_{0.07}Y_{0.10}Ce_{0.15}Zr_{0.68}O_{1.91}$	2.30, 2.81, 2.99, 4.41	7.81, 1.27, 0.92, 1.69	0.10, 0.08, 0.08, 0.11
$Er_{0.05}Y_{0.10}U_{0.10}Zr_{0.75}O_{1.92}$	2.25, 2.38, 2.75, 2.90, 4.39	3.96, 3.17, 2.05, 2.81, 5.54	0.06, 0.08, 0.05, 0.05, 0.09

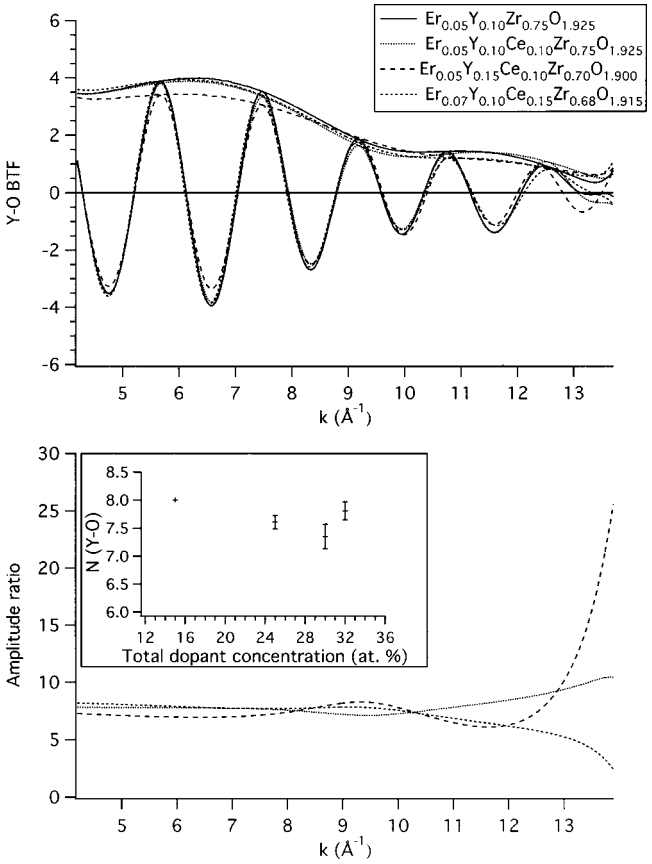

FIG. 5. Upper panel: The imaginary part and amplitude of the backtransform of the NN Y-O shell. The Y-O backtransforms are much more insensitive to the sample composition. Lower panel: The amplitude ratios for the Y-O backtransforms show a much more linear form over the entire *k* range. The inset shows that the Y coordination differs from 8 by less than 10%.

the single Gaussian distribution found for the Y-O distribution.

As was the case with the Zr-O distribution, the Y-O distribution was also found to contain contributions beyond the first shell. Analysis of the fit residuals has identified Y-O distances lying at 2.80 and 3.00 Å, slightly longer than the long *M*-O distances associated with Zr. There is some suggestion that the oxygen distribution around Y is composition dependent, with a larger splitting in the longer distances for compounds where Y is the dominant dopant.

C. Er-O

The NN Er-O distribution is found to be very similar to that of Y-O distribution with a single Gaussian component

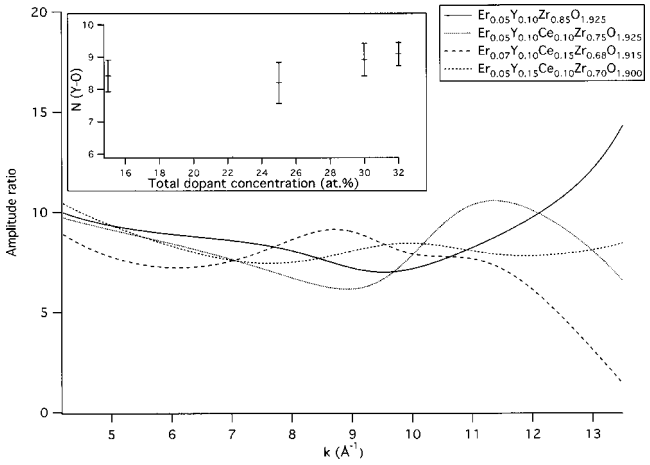

FIG. 6. The amplitude ratios of the Y-O backtransforms with the Zr-O backtransforms. The nonlinearity of the amplitude ratios reflects the difference in backscattering amplitudes as well as the local atomic distribution. The inset shows the results of the coordination number analysis and indicates that the Y coordination is approximately 8 with less than 11% variation as a function of sample composition.

located at 2.29 Å (Table III). The numbers and Debye-Waller factors are both slightly lower for the Er-O distribution indicating better ordering of the NN oxygen distribution. The ratio analysis (Fig. 7) for this oxygen shell, again using the $Er_{0.05}Y_{0.10}Zr_{0.85}O_{1.92}$ sample as the reference and assuming an Er coordination of eight for this compound, indicates that there is a less than 4% deviation from eightfold coordination as a function of dopant concentration. An examination of the highly linear form of the amplitude ratios also demonstrates that the Er-O distribution changes very little as a function of total dopant concentration and is well characterized by a single Gaussian shell. Longer Er-O distances like those found for Zr-O and Y-O are of negligible number.

D. Ce-O

The Ce-O distribution shows the most complicated structure of all the cations. The $Er_{0.05}Y_{0.10}Ce_{0.10}Zr_{0.75}O_{1.92}$ sample shows approximately equal oxygen contributions at 2.22, 2.33, and 2.88 Å (Table IV). The $Er_{0.07}Y_{0.10}Ce_{0.15}Zr_{0.68}O_{1.91}$, and $Er_{0.05}Y_{0.15}Ce_{0.10}Zr_{0.70}O_{1.90}$ samples show a dominant contribution at 2.29 Å with small, almost negligible contributions above and below this main oxygen shell. The complicated structure of the NN oxygen distribution did not al-

TABLE III. Curve fitting results for the Er-O distributions. Typical errors are ±0.02 Å for the bond distances, ±20% for coordination numbers, and ±0.01 for the Debye-Waller factors.

	Er-O (Å)	*N*	σ (Å)
$Er_{0.05}Y_{0.10}Zr_{0.85}O_{1.92}$	2.29, 2.99, 4.28	6.59, 0.54, 6.00	0.09, 0.10, 0.09
$Er_{0.05}Y_{0.10}Ce_{0.10}Zr_{0.75}O_{1.92}$	2.29, 2.85, 4.26	7.68, 0.58, 6.00	0.10, 0.06, 0.07
$Er_{0.05}Y_{0.15}Ce_{0.10}Zr_{0.70}O_{1.90}$	2.28, 2.42, 3.03, 4.33	5.44, 1.09, 0.88, 6.00	0.08, 0.10, 0.09, 0.08
$Er_{0.07}Y_{0.10}Ce_{0.15}Zr_{0.68}O_{1.91}$	2.29, 2.85, 4.29	6.80, 0.32, 6.00	0.09, 0.06, 0.07
$Er_{0.05}Y_{0.10}U_{0.10}Zr_{0.75}O_{1.92}$	2.29, 2.45, 3.04, 4.34	5.44, 1.58, 0.96, 6.00	0.08, 0.09, 0.09, 0.09

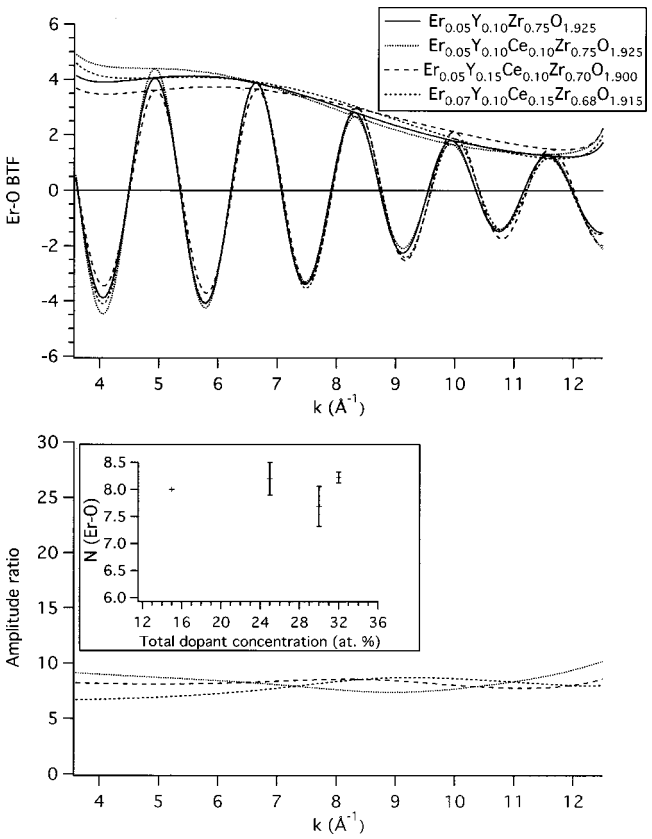

FIG. 7. Upper panel: The backtransforms for the Er-O distribution showing very little change as a function of dopant concentration. Lower panel: The highly linear behavior of the amplitude ratios over the entire *k* range indicate that the Er-O local atomic structure is well characterized by a Gaussian distribution. Analysis of the Er coordination numbers show less than a 4% departure from eight fold coordination.

low for a ratio analysis or a reasonably definitive determination of the Ce coordination.

The *M*-O distributions described above are indicative of local atomic structure that is quite complicated and a function of the neighboring cation. The long *M*-O distances identified around Zr, Y, and Ce to a lesser extent, may result from the presence of large local strains resulting from atomic size mismatch and/or the presence of defect structures that significantly deviate from the crystallographic structure.[46]

The discussion of the general trends of the *M*-O peak amplitudes as a function of the atomic number of the absorbing atom in XAFS alluded too earlier in this section can now be addressed. The presence of multiple *M*-O distances, identified through the fit residuals, around Zr, Y, and Ce result in significant interference between the individual contributions to the XAFS spectrum reducing the peak amplitudes.

E. *M*-*M*

Interpreting the results for the next NN cations is problematic. Relative numbers of the different elements cannot be fixed since it is not known if the local composition is purely random or if there is partial chemical ordering reflecting vacancy allocations and the interaction of the local strain fields resulting from ionic size mismatch. Consequently, curve fits were begun with a single Zr shell and then the various components in the difference spectra were examined vis-à-vis all of the different possible contributions. Again in contrast to XAFS studies of binary CSZ that utilized simple structural models, quite complicated total distributions are found (Fig. 3 and Tables V–VIII).

Zr displays small contributions both above and below the main Zr-*M* distance of 3.54 Å (Table V). The primary Zr-*M* contribution at an average distance of 3.54 Å shows a systematic reduction in amplitude (reflected in the curve-fitting analysis as a decrease in *N*) as the total dopant concentration increases. This decrease in amplitude is accompanied by the increase in amplitude of the shorter Zr-*M* peak found at 3.28 Å. An examination of the relative contributions to the Zr-*M* distribution (Table V) indicates that the addition of Ce increases the population of Zr sites with multiple Zr-*M* bond distances.

The Y-*M* distribution appears more generally disordered around the main Y-Zr contribution at 3.59 Å with additional contributions lying above and below (Table VI). The amplitude of the main Y-*M* peak at 3.59 Å is significantly stronger than the main Zr-*M* contribution at 3.54 Å, indicating less static disorder in the Gaussian component of the Y-*M* contribution. This is reflected in the larger numbers found for this shell with Debye-Waller factors comparable to the main Zr-*M* shell (see Tables V and VI). The disorder in the Y-*M* distribution appears to increase when Ce is added as a dopant, as evidenced by the increased numbers found in the curve fits for the Y-*M* contributions above and below the main Y-*M* distance.

The cation distribution around Er is split between two well-resolved sites, with increased disorder or smaller numbers at the longer distance in compounds where Y is the dominant dopant. The first Er-*M* contribution consists of two closely spaced peaks at a mean distance of 3.62 Å while the second contribution lies at an average distance of 3.97 Å (Table VII). This significant splitting of the Er-*M* peak is unique among the cations present in these IMF compounds. The presence of this splitting and the absence of the long *M*-O bonds found for Zr and Y indicates the preference of Er for relieving local strain by distorting its next NN cation distributions instead of its NN oxygen distribution.

A dominant Ce-*M* peak at 3.62 Å characterizes the cation distribution around Ce. While there is some suggestion in the fit residuals for Ce-*M* distances below this main contribution, these are found to have insignificant spectral weight (Table VIII). The Ce-*M* distribution is by far the most ordered of the cations in that it does not display the small populations of shorter and longer *M*-*M* distances like Zr and Y and does not show the pronounced splitting of the *M*-*M* distances as was found for Er. The addition of Ce to the cubic stabilized structure appears to induce distortions in the Z/Y/Er-*M* shells while leaving the Ce-*M* distribution more ordered.

Given that Ce is often used to simulate the effect of actinides on the structure of CSZ's for IMF applications, it is important to know whether the local atomic environment of U differs appreciably from that of Ce. The FTM's

TABLE IV. Curve fitting results for the Ce/U-O distributions. Typical errors are ±0.02 Å for the bond distances, ±20% for coordination numbers, and ±0.01 for the Debye-Waller factors.

	Ce/U-O (Å)	*N*	σ (Å)
$Er_{0.05}Y_{0.10}Ce_{0.10}Zr_{0.75}O_{1.92}$	2.22, 2.33, 2.88, 4.25	2.21, 2.49, 2.33, 1.96	0.07, 0.07, 0.09, 0.08
$Er_{0.05}Y_{0.15}Ce_{0.10}Zr_{0.70}O_{1.90}$	2.09, 2.29, 2.52, 4.24	0.89, 7.80, 1.30, 1.89	0.07, 0.09, 0.08, 0.07
$Er_{0.07}Y_{0.10}Ce_{0.15}Zr_{0.68}O_{1.91}$	2.05, 2.28, 2.43, 2.95, 4.27	0.71, 6.82, 1.12, 0.54, 1.40	0.08, 0.09, 0.07, 0.09, 0.08
$Er_{0.05}Y_{0.10}U_{0.10}Zr_{0.75}O_{1.92}$	2.36, 2.95	4.84, 2.54	0.10, 0.10

TABLE V. Curve fitting results for the Zr-*M* distributions. Typical errors are ±0.02 Å for the bond distances, ±20% for coordination numbers, and ±0.01 for the Debye-Waller factors.

	Zr-*M* (Å)	*N*	σ (Å)
$Er_{0.05}Y_{0.10}Zr_{0.85}O_{1.92}$	3.27, 3.57, 3.87	0.23, 11.77, 0.64	0.07, 0.11, 0.09
$Er_{0.05}Y_{0.10}Ce_{0.10}Zr_{0.75}O_{1.92}$	3.28, 3.53, 3.85	1.86, 10.14, 0.66	0.10, 0.11, 0.09
$Er_{0.05}Y_{0.15}Ce_{0.10}Zr_{0.70}O_{1.90}$	3.29, 3.53, 3.85	2.15, 9.85, 0.92	0.10, 0.11, 0.09
$Er_{0.07}Y_{0.10}Ce_{0.15}Zr_{0.68}O_{1.91}$	3.28, 3.54, 3.87, 4.40	1.83, 7.71, 0.43, 1.04	0.10, 0.11, 0.09, 0.09
$Er_{0.05}Y_{0.10}U_{0.10}Zr_{0.75}O_{1.92}$	3.32, 3.57, 3.71	1.54, 10.46, 0.20	0.10, 0.06, 0.09

TABLE VI. Curve fitting results for the Y-*M* distributions. Typical errors are ±0.02 Å for the bond distances, ±20% for coordination numbers, and ±0.01 for the Debye-Waller factors.

	Y-*M* (Å)	*N*	σ (Å)
$Er_{0.05}Y_{0.10}Zr_{0.85}O_{1.92}$	3.36, 3.59, 4.24	0.62, 15.23, 0.50	0.09, 0.10, 0.06
$Er_{0.05}Y_{0.10}Zr_{0.75}O_{1.92}$	3.34, 3.59, 4.38	2.45, 16.60, 6.04	0.10, 0.11, 0.15
$Er_{0.05}Y_{0.15}Ce_{0.10}Zr_{0.70}O_{1.90}$	3.36, 3.58, 4.24	3.69, 19.92, 7.19	0.10, 0.11, 0.13
$Er_{0.07}Y_{0.10}Ce_{0.15}Zr_{0.68}O_{1.91}$	3.34, 3.62, 3.79	0.91, 11.06, 2.73	0.10, 0.10, 0.10
$Er_{0.05}Y_{0.10}U_{0.10}Zr_{0.75}O_{1.92}$	3.60	20.69	0.11

TABLE VII. Curve fitting results for the Er-*M* distributions. Typical errors are ±0.02 Å for the bond distances, ±20% for coordination numbers, and ±0.01 for the Debye-Waller factors.

	Er-*M* (Å)	*N*	σ (Å)
$Er_{0.05}Y_{0.10}Zr_{0.85}O_{1.92}$	3.59, 3.63, 4.00	7.42, 4.90, 1.68	0.09, 0.14, 0.09
$Er_{0.05}Y_{0.10}Ce_{0.10}Zr_{0.75}O_{1.92}$	3.57, 3.58, 3.94	6.79, 3.64, 3.57	0.07, 0.09, 0.09
$Er_{0.05}Y_{0.15}Ce_{0.10}Zr_{0.70}O_{1.90}$	3.63, 3.66, 3.99	6.27, 5.88, 1.85	0.08, 0.10, 0.09
$Er_{0.07}Y_{0.10}Ce_{0.15}Zr_{0.68}O_{1.91}$	3.59, 3.65, 3.95	5.55, 4.26, 6.19	0.08, 0.10, 0.10
$Er_{0.05}Y_{0.10}U_{0.10}Zr_{0.75}O_{1.92}$	3.62, 3.63, 4.00	4.40, 8.10, 1.50	0.10, 0.08, 0.09

TABLE VIII. Curve fitting results for the Ce/U-*M* distributions. Typical errors are ±0.02 Å for the bond distances, ±20% for coordination numbers, and ±0.01 for the Debye-Waller factors.

	Ce/U-*M* (Å)	*N*	σ (Å)
$Er_{0.05}Y_{0.10}Ce_{0.10}Zr_{0.75}O_{1.92}$	3.30, 3.62	0.88, 7.56	0.09, 0.09
$Er_{0.05}Y_{0.15}Ce_{0.10}Zr_{0.70}O_{1.90}$	3.24, 3.62	0.27, 7.27	0.05, 0.08
$Er_{0.07}Y_{0.10}Ce_{0.15}Zr_{0.68}O_{1.91}$	3.28, 3.63	0.56, 4.95	0.09, 0.08
$Er_{0.05}Y_{0.10}U_{0.10}Zr_{0.75}O_{1.92}$	3.4, 3.74	3.85, 6.97	0.10, 0.10

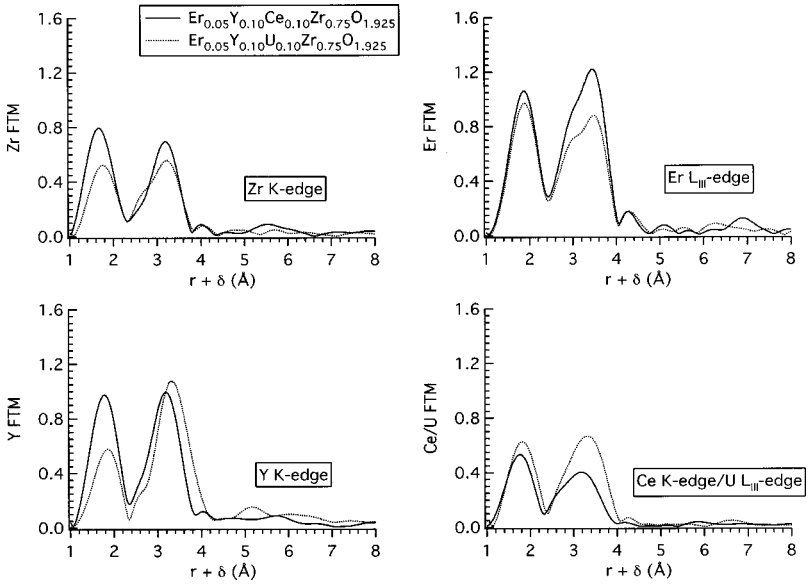

FIG. 8. The FTM's of the XAFS data for the Y-10 Er-5 Ce/U-10 IMF compounds. These data indicate that Ce and U affect their local atomic environments differently in these CSZ compounds. The Zr, Y, and Ce data show significant changes upon substitution of U for Ce indicating a corresponding difference in their local atomic structure. The Er data show little change aside from some amplitude reduction in the Er-*M* peak.

for the IMF compounds $Er_{0.05}Y_{0.10}Ce_{0.10}Zr_{0.75}O_{1.92}$ and $Er_{0.05}Y_{0.10}U_{0.10}Zr_{0.75}O_{1.92}$ are compared in Fig. 8.

The Zr-O peak displays a highly reduced amplitude and a 0.10 Å shift to longer distance. Likewise, the Zr-*M* peak also shows reduced amplitude but, in addition, displays a prominent shoulder on the low-*r* side. The effect of U substitution for Ce on the Y-O peak is similar to that of Zr-O; the peak amplitude is reduced and shifted to larger distances by 0.06 Å. The Y-*M* peak is shifted to larger distances by 0.13 Å with a slightly enhanced amplitude upon U substitution. Unlike both the Zr and Y data in the U compound, the Er-O and Er-*M* distributions do not show any significant shift in peak positions or shape. The only effect seen in the Er data is a reduction in amplitude of the Er-*M* peaks. The Ce/U FTM's on the other hand show higher amplitudes in the U-O and U-*M* peaks as well as a shift to larger distances. These results indicate that Ce and U environments in the CSZ lattice are not identical. In addition, one can see that the local atomic structure around each of the cations is affected differently when U is substituted for Ce.

The RDF's generated from the curve fitting analysis (Fig. 9) indicate the general trend of expansion of the oxygen and cation peaks away from the central cation when Ce is replaced by U with two important exceptions (Tables I–VIII). The local atomic environment around Y shows significant changes when U is substituted for Ce. The single Gaussian Y-O peak found in the Ce compound is split into two approximately equal contributions at 2.25 and 2.38 Å. In addition, the longer Y-O peaks lying above the NN oxygens show increased amplitudes with more pronounced splitting. The Y-*M* peak becomes distinctly more Gaussian in shape indicating less disorder in the Y-*M* distribution when U is substituted for Ce. The other significant effect of U substitution is found in the Ce/U-*M* distribution. The Ce-*M* distribution shows a single Ce-*M* contribution at 3.62 Å while the U-*M* distribution is split into two contributions at 3.44 and 3.74 Å. There appears to be a significant, element-specific difference in the way Ce and U affect their local atomic environments. The significant distortions around U seem to lie in the next

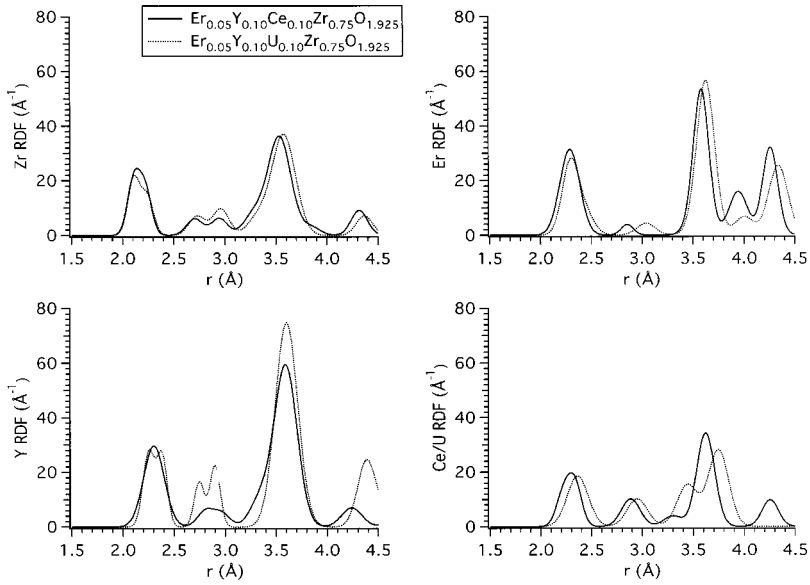

FIG. 9. The RDF's resulting from curve fits to the Ce/U-CSZ IMF compounds. The larger size of U(IV) relative to Ce(IV) (cf. NN oxygen positions in Ce/U plot) results in an expansion of the second and third NN for Zr and Er, whose RDF's are otherwise very similar in both the Ce and U compounds. The substantial differences in the Y environment, including splitting of the oxygen shell at 2.3 and increased separation of the more distant set of oxygen atoms, and in the Ce/U including the splitting of the second-shell cations, imply a strong interaction between the Y and U sites.

NN cation shells while those around Ce seem to lie in the NN oxygen shells. Ratio analysis of the NN oxygen shells for Zr, Y, and Er indicate no significant changes in coordination number when U is substituted for Ce.

These results suggest that the Y and U local environments interact strongly. Cooperative behavior of this type has previously only been reported for cations smaller than Zr^{4+}, so this finding suggests that U, and other actinides, experience novel interactions with specific cations. The U next NN cation distribution significantly differs from that of Ce and induces a simple expansion of the oxygen and cation shells surrounding Zr and Er.

IV. CONCLUSIONS

Previous XAFS studies of CSZ concluded with stabilization models based on simple dichotomies, aliovalent vs isovalent, dopant cations larger than Zr^{4+} vs smaller, and oxygen vacancy ordering. These suggest simple, non-element-specific origins such as steric constraints for their effects. Expanding both the range of elements and the model used in the analysis demonstrates that such models for the atomic structure of CSZ are incomplete.

The first significant result of our XAFS study is the finding that the cations in CSZ do not behave identically with respect to distortions in their environments. The results presented here imply highly element-specific mechanisms for compensating atomic radius-lattice mismatch, either by distorting the NN oxygen or next NN cation distributions. Zr, Y, and Ce all have highly distorted oxygen distributions while Er, despite its similarity to Y in size and charge, displays a single Gaussian oxygen distribution. The next NN cation distributions around Zr and Y become significantly more disordered when Ce is added as a dopant while Ce itself is found to have a single well-ordered Gaussian distribution of next NN cations. The next NN cations of Er show a split distribution in all compounds. The effect of U substitution in general, appears as an expansion of the oxygen and cation shells away from their positions in the Ce compound. An important exception is the behavior of the local atomic structure around Y, where introduction of U enhances the distortions in the oxygen distribution and reduces the disorder of the surrounding cations. The Ce/U-*M* distributions also differ in that the Ce-*M* RDF consists of a single Gaussian contribution while that of U is split into two U-*M* distances.

Second, we have found that collective and cooperative effects must be considered. In the ternary and Ce-containing compounds these are suggested especially by the changes in the RDF's (the Y-O and Er-*M* distributions) of some of the elements to the Y fraction of the total dopant level as well as the observation that addition of Ce induces distortions to the next NN cation distributions around Zr and Y. A special role for Y in cooperative behavior is also implied by the radical changes in its RDF prompted by the replacement of Ce with U. Cooperative and/or collective effects between specific cation pairs can result in the formation of nanometer-scale defect structures and/or cation ordering that could have significant ramifications on the proposed mechanisms for stabilization of the cubic and tetragonal phases of zirconia. Currently, proposed stabilization mechanisms typically include simple displacements of oxygen atoms and cations with respect to the crystallographic fluorite structure resulting from the introduction of oxygen vacancies.

In summary, cation-specific defect structures, response to local strain, and atomic-scale collective rather than isolated behavior appear to be an important feature in CSZ that has not been addressed in currently proposed stabilization mechanisms.

ACKNOWLEDGMENTS

XAFS experiments were performed at the Stanford Synchrotron Radiation Laboratory, which is operated by the U.S. Department of Energy, Office of Basic Energy Sciences. This research was supported by DOE/OBES under Contract No. W-7405.

[1] Shih-Ming Ho, Mater. Sci. Eng. **54**, 23 (1982).
[2] S. D. Conradson, Appl. Spectrosc. **52**, 252A (1998).
[3] L. M. Colyer, G. N. Greaves, S. W. Carr, and K. K. Fox, J. Phys. Chem. B **101**, 10 105 (1997).
[4] E. D. Bauer, F. Bridges, C. H. Booth, J. B. Boyce, T. Claeson, G. Brorsson, and Y. Suzuki, Phys. Rev. B **54**, 13 352 (1996).
[5] T. A. Tyson, S. D. Conradson, R. F. C. Farrow, and B. A. Jones, Phys. Rev. B **54**, R3702 (1996).
[6] J. M. Tranquada, B. J. Sternlieb, J. D. Axe, Y. Nakamura, and S. Uchida, Nature (London) **375**, 561 (1995).
[7] A. Bianconi, N. L. Saini, A. Lanzara, M. Missori, T. Rossetti, H. Oyanagi, H. Yamaguchi, K. Oka, and T. Ito, Phys. Rev. Lett. **76**, 3412 (1996).
[8] H. Chen, S. Mori, and S.-W. Cheong, J. Phys. IV **9**, 307 (1999).
[9] K. Smith and H. W. Newkirk, Acta Crystallogr. **18**, 983 (1965).
[10] K. Smith and C. F. Cline, J. Am. Ceram. Soc. **45**, 249 (1962).
[11] G. Teufer, Acta Crystallogr. **15**, 1187 (1962).
[12] D. Steele and B. E. F. Fender, J. Phys. C **7**, 1 (1974).
[13] D. Michael, L. Mozerolles, M. Pez, and Y. Jorba, J. Mater. Sci. **18**, 2618 (1983).
[14] J. Lefevre, Ann. Chim. (Paris) **8**, 117 (1963).
[15] T. H. Etsell and S. N. Flengas, Chem. Rev. **70**, 339 (1970).
[16] M. Yoshimura, Am. Ceram. Soc. Bull. **67**, 1950 (1988).
[17] P. Li, I-W. Chen, and J. E. Penner-Hahn, Phys. Rev. B **48**, 10 063 (1993).
[18] P. Li, I-W. Chen, and J. E. Penner-Hahn, Phys. Rev. B **48**, 10 074 (1993).
[19] P. Li, I-W. Chen, and J. E. Penner-Hahn, J. Am. Ceram. Soc. **77**, 118 (1994).
[20] M. Weller, Z. Metallkd. **84**, 381 (1993).
[21] D. Komyoji, A. Yoshiasa, T. Moriga, S. Emura, F. Kanamaru, and K. Koto, Solid State Ionics **50**, 291 (1992).
[22] H. Morikawa, Y. Shimizugawa, F. Marumo, T. Harasawa, H. Ikawa, K. Tohji, and Y. Udagawa, J. Ceram. Soc. Jpn. **96**, 253 (1988).

[23] B. W. Veal, A. G. Mckale, A. P. Paulikas, S. J. Rothman, and L. J. Nowicki, Physica B **150**, 234 (1988).
[24] M. H. Tuilier, J. Dexpert-Ghys, and P. Lagarde, J. Solid State Chem. **69**, 153 (1987).
[25] C. R. A. Catlow, A. V. Chadwick, G. N. Greaves, and L. M. Moroney, J. Am. Ceram. Soc. **69**, 272 (1986).
[26] G. Stapper, M. Bernasconi, N. Nicoloso, and M. Parrinello, Phys. Rev. B **59**, 797 (1999).
[27] P. Li, I-W. Chen, and J. E. Penner-Hahn, J. Am. Ceram. Soc. **77**, 1281 (1994).
[28] P. Li, I-W. Chen, and J. E. Penner-Hahn, J. Am. Ceram. Soc. **77**, 1289 (1994).
[29] D. N. Argyriou, M. M. Elcombe, and Allen C. Larson J. Phys. Chem. Solids **57**, 183 (1996).
[30] R. L. Withers, Th. Proffen, and T. R. Welberry, Philos. Mag. A **79**, 753 (1999).
[31] T. R. Welberry, R. L. Withers, and S. Mayo, J. Solid State Chem. **115**, 43 (1995).
[32] M. Yashima, S. Sasaki, Y. Yamaguchi, M. Kakihana, M. Yoshimura, and T. Mori, Appl. Phys. Lett. **72**, 182 (1998).
[33] D. N. Argyriou, J. Appl. Crystallogr. **27**, 155 (1994).
[34] T. R. Welberry, R. L. Withers, J. G. Tompson, and B. D. Butler, Solid State Chem. **100**, 71 (1992).
[35] T. R. Welberry, B. D. Butler, J. G. Tompson, and R. L. Withers, Solid State Chem. **106**, 461 (1993).
[36] H. Horiuchi, A. J. Schultz, P. C. W. Leung, and J. M. Williams, Acta Crystallogr., Sect. B: Struct. Crystallogr. Cryst. Chem. **40**, 367 (1984).
[37] C. J. Howard, R. J. Hill, and B. E. Reichert, Acta Crystallogr., Sect. B: Struct. Crystallogr. Cryst. Chem. **44**, 116 (1988).
[38] D. N. Argyriou and M. M. Elcombe, J. Phys. Chem. Solids **57**, 343 (1996).
[39] C. Degueldre and S. D. Conradson, Appl. Phys. A (to be published 2001).
[40] D. J. Kim, J. Am. Ceram. Soc. **72**, 1415 (1989).
[41] Boon K. Teo, in *EXAFS: Basic Principles and Data Analysis* (Springer-Verlag, Berlin, 1986).
[42] A. L. Ankudinov and J. J. Rehr, Phys. Rev. B **56**, R1712 (1997).
[43] P. Li, I-W. Chen, and J. E. Penner-Hahn, Phys. Rev. B **48**, 10 082 (1993).
[44] T. A. Tyson, J. Mustre de Leon, S. D. Conradson, A. R. Bishop, J. J. Neumeier, H. Roder, and J. Zang, Phys. Rev. B **53**, 13 985 (1996).
[45] M. Winterer, J. Appl. Phys. **88**, 5635 (2000).
[46] J. P. Goff, W. Hayes, S. Hull, M. T. Hutchings, and K. N. Clausen, Phys. Rev. B **59**, 14 202 (1999).